Exploring the Origins of Improved Photocurrent by Acidic Treatment for Quaternary Tantalum-Based Oxynitride Photoanodes on the Example of $CaTaO_2N$

Zili Ma†, Aleksander Jaworski‡, Janine George⊥, Anna Rokicinska∥, Thomas Thersleff‡, Tetyana M. Budnyak‡, Geoffroy Hautier⊥, Andrew J. Pell‡, Richard Dronskowski†,◊, Piotr Kuśtrowski∥, Adam Slabon*,‡

†Chair of Solid-State and Quantum Chemistry, Institute of Inorganic Chemistry, RWTH Aachen University, Landoltweg 1, D-52056 Aachen, Germany

‡Department of Materials and Environmental Chemistry, Stockholm University, Svante Arrhenius väg 16 C, 106 91 Stockholm, Sweden

⊥Institute of Condensed Matter and Nanosciences, Université Catholique de Louvain, Chemin des Étoiles 8, 1348 Louvain-la-Neuve, Belgium

∥Faculty of Chemistry, Jagiellonian University, Gronostajowa 2, 30-387 Krakow, Poland

◊ Hoffmann Institute of Advanced Materials, Shenzhen Polytechnic, 7098 Liuxian Blvd, Shenzhen, China

ABSTRACT: Quaternary tantalum-based oxynitrides $ATa(O,N)_3$, with electronic band gaps between 1.8 and 2.4 eV, are promising materials for photochemical water-splitting. The tailoring of their surface properties is a critical aspect to obtain efficient hole extraction. We report on the origin of improved photoelectrochemical (PEC) water oxidation by means of acidic treatment for this class of compounds on the example of cubic $CaTaO_2N$ particles. We address the effect of acidic treatment by using complementary physical characterization techniques, such as X-ray photoelectron spectroscopy (XPS), electrochemical impedance spectroscopy (EIS), ^1H and ^{14}N solid-state nuclear magnetic resonance (NMR) spectroscopy, electron microscopy and electronic band structure calculations at the density functional theory (DFT) level. In combination with photoelectrochemical measurements, solid-state NMR indicates that the restructured surface displays a meaningfully higher concentration of terminating OH groups. Subsequent deposition of a nickel borate (NiB_i) catalyst on the acid-treated surface yields a higher percentual upsurge of photocurrent in comparison to pristine $CaTaO_2N$. Our results highlight the application of solid-state NMR spectroscopy for understanding of the semiconductor-catalyst interface in photochemical devices.

INTRODUCTION

An environment-friendly route for sustainable hydrogen production as chemical fuel is PEC water splitting.[1–3] The oxygen evolution reaction (OER), as one of the two half reactions during overall water splitting, is more demanding than the hydrogen evolution reaction (HER) because of inferior charge transport and slower kinetics of a four-electron reaction.[4,5] Progress in PEC water oxidation on photoanodes, i.e. semiconductor thin films coated with OER catalysts, has been mainly driven by oxidic semiconductors.[6] This is due to their chemical stability under operating conditions in neutral and alkaline electrolytes. For instance, the best-performing oxide photoanode is $BiVO_4$, with an electronic bandgap of 2.4 eV being equivalent to a maximum theoretical photocurrent density of 7.4 mA cm^{-2}. Besides oxide materials with narrower band gaps, such as hematite[7,8], nitrogen-based compounds have emerged as semiconductor materials with higher theoretical photocurrent densities.

Semiconducting n-type metal carbodiimides and metal (oxy)nitrides are prospective photoanode candidates due their usually narrower band gaps.[9,10] For instance, the bandgap of Ta_3N_5 is 2.1 eV and the experimentally achieved photocurrents of 12.5 mA cm^{-2} are already very close to the theoretical limit of 12.9 mA cm^{-2}.[11] Nonetheless, the onset potential of 0.6 V vs. the reversible hydrogen electrode (RHE) is still much higher than its flat-band potential of −0.2 V vs. RHE. Quaternary oxynitrides $AB(O,N)_3$ (A = La, Ca, Sr, Ba; B=Ta, Nb) crystallizing with a perovskite-related structure, can exhibit variable band gaps ranging from 1.7 to 2.4 eV depending on their chemical composition.[12–14] Recently, we reported the first successful synthesis of $SrTaO_2N$ nanowires that can be modified with functional coatings to achieve a hole-extraction gradient.[13,15]

Quaternary oxynitrides $ATa(O,N)_3$ generally achieve a higher photocatalytic activity in comparison to their niobium counterparts $ANb(O,N)_3$. This is due to the higher chemical stability of Ta^{5+}, compared to Nb^{5+}, which is more easily reduced to Nb^{4+}. Contrariwise, the high photocatalytic activity of the titanium-based oxynitride $LaTiO_2N$ (E_g = 2.1 eV) is attributed to the existence of Ti^{3+} at the surface region. Domen et al.[16] demonstrated a twofold increase of

photochemical activity for $LaTiO_2N$ by immersing the material, prior to the catalytic test, in aqua regia for a short period of time. This enhancement is believed to originate from surface restructuration under acidic treatment, leading thus to i) removal of inactive surface layer regions and ii) reduction of Ti^{4+} to Ti^{3+} in the rearranged surface region. Acidic treatment was also used as post-synthetic treatment of $BaTaO_2N$ in order to remove excess BaO.[17]

The surface chemistry plays a decisive role for the photocatalytic activity of Ta_3N_5, because its surface consists of reduced tantalum ions forming a 2 nm thick TaN layer. This results in significant recombination of charge carriers at the surface. Acidic treatment can remove this surface layer and leads to an improvement in photocatalytic water-splitting. Interestingly, the presence of oxygen in these etched samples is suggested by the XPS results, but the occurrence of hydroxyl species cannot be proven by infrared spectroscopy.[18]

We report on the origin of improved photoelectrochemical behavior by means of acidic treatment for quaternary Ta-based oxynitrides on the example of $CaTaO_2N$. The title compound can be classified as a semiconductor chemically lying between Ta_3N_5 and $LaTiO_2N$. $CaTaO_2N$ crystallizes with a perovskite-related structure (space group *Pnma*) and has a band gap of 2.4 eV. The compound can be applied as a photocatalyst for either water-splitting[19–21] or CO_2 reduction[22], as well as non-toxic yellow pigment.[23] We report on the first fabrication of a $CaTaO_2N$ photoanode and address the effect of acidic treatment by using complementary physical characterization techniques, such as X-ray photoelectron spectroscopy (XPS), EIS, ^1H and ^{14}N solid-state NMR spectroscopy, and electronic band structure calculations at the density functional theory (DFT) level.

EXPERIMENTAL SECTION

Synthesis of $CaTaO_2N$. The oxide precursor $Ca_2Ta_2O_7$ was synthesized by solid state reaction of $CaCO_3$ (99 wt.-%, Grüssing GmbH) and Ta_2O_5 (99.85 wt.-%, abcr GmbH). The mixture was heated at 1343 K for 24 h at a ramping rate of 10 K min^{-1} under ambient atmosphere and then cooled to room temperature at a rate of 10 K min^{-1}.

For the conversion to $CaTaO_2N$, 700 mg as-prepared white $Ca_2Ta_2O_7$ powder was mixed with a flux of 300 mg NaCl (99.5 wt.-%, Grüssing GmbH) and 300 mg KCl (99.5 wt.-%, Grüssing GmbH). For ammonolysis, the mixed powder was placed into an alumina crucible in a tube furnace and was subsequently heated under a constant flow of NH_3 (15 mL min^{-1}) and H_2 (5 mL min^{-1}) at 1273 K for 15 h at a ramping rate of 10 K min^{-1}. After cooling to room temperature, the product was washed thoroughly and filtered with distilled water to completely remove the flux agents. The yellow product was dried in an oven at 333K for 8 h.

Etching of $CaTaO_2N$ powders. 200 mg $CaTaO_2N$ was added into 4 ml fresh prepared aqua regia from HCl (~37%, Fisher Chemical) and HNO_3 (65%, Fisher Chemical) and the suspension was stirred for 20 seconds. Afterwards, the suspension was poured immediately into 1 L of distilled water, rinsed thoroughly during subsequent filtration and dried in an oven at 333K for 8 h. The sample was denoted as $CaTaO_2N$-A.

Preparation and etching of $SrNbO_2N$ powder. $SrNbO_2N$ was synthesized via flux-assisted nitridation method. Briefly, 204.8 mg Nb_2O_5 (99.9 wt.-%, Sigma-Aldrich), 227.5 mg $SrCO_3$ (99 wt.-%, Alfa Aesar) and 567.9 mg $SrCl_2{\cdot}6H_2O$ (flux; 99 wt.-%, Riedel-de Haën) were ground. The previous mixture was placed in an alumina crucible and heated under a constant flow of NH_3 (15 mL min^{-1}) and H_2 (5 mL min^{-1}) at 1173 K for 15 h at a heating rate of 10 K min^{-1}. After cooling to room temperature, the product was washed thoroughly and filtered with distilled water to completely remove the flux agents, and dried at 333 K for 8 h. The acidic treatment was the same as for $CaTaO_2N$ powder. The powder XRD are presented in Figure S1.

Fabrication of $CaTaO_2N$ photoanodes. Thin film photoanodes were fabricated via electrophoretic deposition (EPD) process followed by necking treatment. In short, 24 mg as-prepared $CaTaO_2N$ or $CaTaO_2N$-A were mixed with 6 mg of iodine in 30 ml of acetone, followed by 30 min sonication to obtain a uniform suspension. Two pre-cleaned conductive fluorine-doped tin oxide (FTO) slides or one FTO slide and one titanium sheet were immersed in the above suspension with 1 cm distance, and a potential of 25 V was applied between them for 4 min. $CaTaO_2N$ particles were deposited on the electrode. After the electrodes were dried in air, 10 µl of 10 mM $TaCl_5$ (99 wt.-%, abcr GmbH) methanol solution was dropped on the electrodes and dried. This procedure was repeated four times followed by annealing at 723 K for 1 h under a constant flow of NH_3 (15 mL min^{-1}) and H_2 (5 mL min^{-1}).

Electrodeposition of NiB_i overlayer. Electrodeposition of NiB_i[24] onto $CaTaO_2N$ photoanodes was done in a electrolyte containing 1 mM $Ni(NO_3)_2$ and 0.1 M potassium borate (KB_i) buffer at pH 9.2 at a constant potential of 1.21 V vs. 1 M Ag/AgCl for 15 s. The electrode was subsequently washed with deionized water. Scheme 1 shows the complete preparation procedure for the Ti/$CaTaO_2N$-A/NiB_i photoanode.

Powder X-ray Diffraction (XRD). Powder XRD reflection patterns were recorded on a STOE STADI-P diffractometer (Cu $K_{\alpha1}$ radiation) equipped with a DECTRIS Mythen 1K detector in transmission mode.

UV–Vis Spectroscopy. The UV–vis spectra were recorded with a Shimadzu UV-2600 spectrophotometer using $BaSO_4$ as the reference.

Solid State Nuclear Magnetic Resonance (NMR). The ^1H and ^{14}N magic angle spinning (MAS) NMR experiments were performed at the magnetic field B_0 = 14.1 T (Larmor frequencies of 600.12 and 43.36 MHz for ^1H and ^{14}N, respectively) and MAS rate ν_r = 60.00 kHz on a Bruker Advance-III spectrometer equipped with 1.3 mm MAS probehead. The ^1H acquisitions involved rotor-synchronized, double-adiabatic spin-echo sequence with 90° 1.25 µs excitation pulse followed by two 50.0 µs tanh/tan high-power adiabatic pulses (SHAPs) with 5 MHz frequency sweep.[25–27] All pulses operated at the nutation frequency ν_{nut} = 200 kHz. 1024 signal transients with 5 s relaxation delay were accumulated for each spectrum. The relaxation delay of 5 s together with the total pulse sequence duration of 133 µs

were used and verified to provide quantitative spectra. Shifts were referenced with respect to neat tetramethylsilane (TMS). The ^{14}N NMR spectra were recorded with single-pulse ("Bloch-decay") protocol using 3.0 µs excitation pulse with the nutation frequency of 78 kHz. 65536 scans with 1 s relaxation delay were collected for each spectrum. ^{14}N shifts were referenced with respect to solid NH_4Cl.

X-ray Photoelectron Spectroscopy (XPS). XPS spectra were recorded by a hemispherical VG SCIENTA R3000 analyzer using a monochromatized aluminum source Al K_α (E = 1486.6 eV) at constant pass energy of 100 eV. The binding energies were referenced to the C 1s core level (E_b = 284.6 eV). The composition and chemical surrounding of the sample surface were determined on the basis of the areas and binding energies of Na 1s, Ni 2p, Ca 2p, B 1s, O 1s, N 1s, C 1s, Ta 4p and Ta 4f photoelectron peaks. The fitting of high-resolution spectra was obtained through the Casa XPS software.

Scanning electron microscopy (SEM) and Transmission Electron Microscopy (TEM). SEM images were acquired on a Leo Supra 35VP SMT (Zeiss). To investigate the chemical homogeneity and morphology, a TEM sample was prepared by mechanically removing a part of the $CaTaO_2N$ particles from the photoanode. The sample was investigated with a Themis Z TEM (Thermo Fisher) equipped with a SuperX EDX detector operated at 300 kV in Scanning Transmission Electron Microscopy (STEM) mode.

Computational details. Based on the structural determination of ref[28], 30 model structures for $CaTaO_2N$ with different anion order and assumed ordered compounds were built: we used a 1 x 1 x 1 cell, filled the 4c positions with 2 O and 2 N, and the 8d positions with 6 O and 2 N, tested all possibilities, and identified symmetrically different structures with the help of pymatgen.[29] Furthermore, the predicted structure of Wolff and Dronskowski for $CaTaO_2N$ was also compared to our structural models.[30] All 31 structural optimizations and the calculations of the wavefunctions for the bonding analysis of all 31 structures were calculated with periodic DFT in VASP[31,32] with strict convergence criteria of $\Delta E < 10^{-7}$ (10^{-5}) eV per cell for electronic (structural) optimizations, respectively. We used the projector augmented-wave method[31,32] with a plane wave cutoff of 520 eV and the Perdew–Burke–Ernzerhof (PBE) functional.[33]

The Integrated Crystal Hamilton Overlap Population (ICOHP) values and Crystal Hamilton Overlap Populations (COHPs) were calculated with the help of Lobster 3.1.0.[34–37] The following basis functions of the pbeVasp-Fit2015 basis set was used: 2s and 2p for O and N, 3s, 3p, and 4s for Ca, and 5p, 5d, and 6s for Ta.

Photoelectrochemical measurements. Photoelectrochemical studies of the $CaTaO_2N$ particle-based photoanodes were measured in 0.1 M NaOH aqueous solution (pH 13) with a three-electrode system where a Pt wire and 1 M Ag/AgCl electrode were used as a counter electrode and reference electrode, respectively, under AM 1.5G simulated sunlight. The Nernst equation ($E_{RHE} = E^{\theta}_{Ag/AgCl} + 0.059$ pH + $E_{Ag/AgCl}$) was used to convert all measured potentials vs. Ag/AgCl reference electrode to the potentials vs. RHE. The AM 1.5G simulated solar illumination was generated by a solar light simulator (class-AAA 94023A, Newport) with an ozone-free 450 W xenon short-arc lamp. Linear sweep voltammetry (LSV) from 0.0 to 1.3 V vs. RHE with a scan rate of 10 mV/s and chronoamperometry curves at a constant bias 1.23 vs. RHE were recorded with a potentiostat (PalmSens4, PalmSens BV). Mott-Schottky measurements were conducted in 0.1 M NaOH using the Gamry INTERFACE 1010T Potentiostat/Galvanostat/ZRA workstation in a dark setting at AC amplitude of 5 mV and a frequency of 10 Hz. The electrochemical impedance spectroscopy (EIS) was measured at 1.0 V vs RHE in the a.c. potential frequency range of 20 kHz-0.2 Hz under an AM 1.5G illumination.

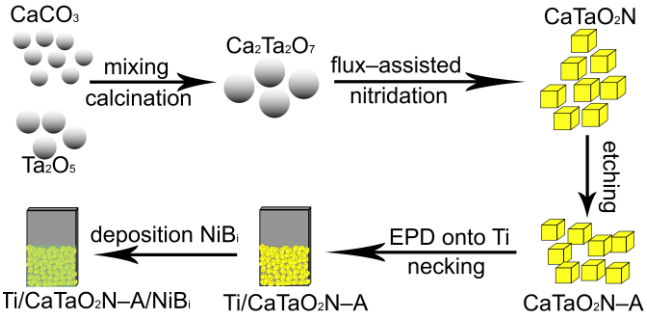

Scheme 1. Schematic illustration of the preparation of $CaTaO_2N$ particle-based photoanodes.

RESULTS AND DISCUSSION

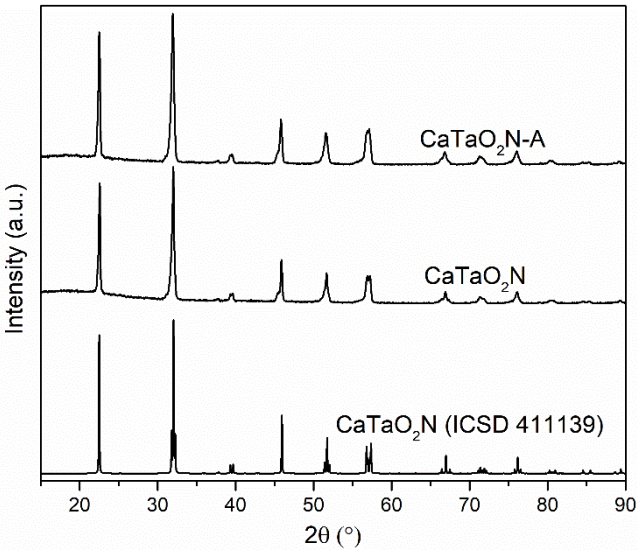

Figure 1. Experimental and simulated powder XRD patterns of $CaTaO_2N$ and $CaTaO_2N$-A (ICSD 411139).

Structural Characterization. XRD patterns confirm the successful synthesis of the precursor $Ca_2Ta_2O_7$ (Figure S2) and conversion to the perovskite-related structure of $CaTaO_2N$ as a single phase (Figure 1). No distinct differences in the diffraction angles and peak intensities were observed after the aqua regia treatment in the XRD patterns. This structural stability is similar to $LaTiO_2N$ if the acid-treatment is carried out only for a short period of time, i.e. up to few minutes.[16] The UV-vis absorption edge for $CaTaO_2N$ and $CaTaO_2N$-A is almost the same and around 500 nm (Figure S3); in agreement with the known value of $CaTaO_2N$.[21]

SEM was employed to observe the morphology of the fabricated $CaTaO_2N$ photoanode. The electrode surface is covered by cubic particles in the nano- to micrometer range (Figure 2). The cubes also exhibit several pores, which is a known phenomenon occurring when transforming oxides into nitrides or oxynitrides.

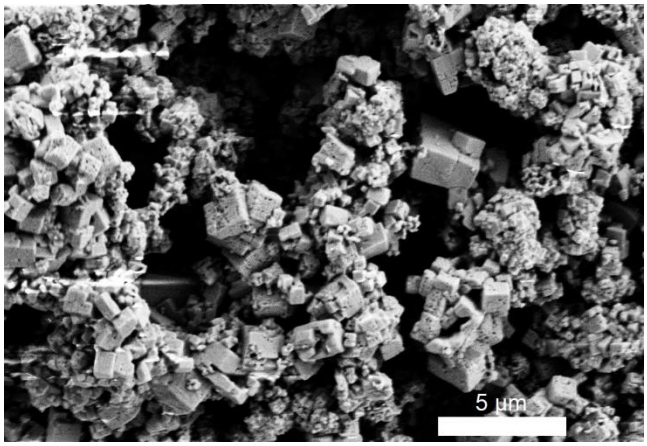

Figure 2. SEM micrograph of a $CaTaO_2N$ photoanode on Ti substrate.

Aqua regia has been reported to enhance the photocatalytic performance of $LaTiO_2N$[16] and Ta_3N_5[18] by removal of the inactive surface layers. However, for both reported cases the applied analytic techniques including XPS and FT-IR spectroscopy did not show any evidence for the presence of surface hydroxyl groups after acidic treatment. This lack of quantitative description of the etching effect for these two materials is due to the low sensitivity toward changes in the composition occurring at the surface. For the binary nitride, the enhancement in photochemical activity is believed to be a consequence of etching a TaN or amorphous TaO surface layer. In order to understand the origin of enhanced photoelectrochemical performance for a quaternary oxynitride, we analyzed the photoanode by solid-state NMR.[38]

In Figure 3a the quantitative ^{1}H MAS NMR spectra collected from as-synthesized and aqua-regia-treated $CaTaO_2N$ perovskite oxynitrides are shown. It should be noted that the spectra were acquired before the oxynitride was assembled into a thin film electrode. The untreated sample exhibits ^{1}H signal patterns typical for inorganic surfaces with proton species in terminating hydroxyl moieties with a chemical shift around 1 ppm, as well as those from different adsorbed water layers (4–7 ppm). The ^{1}H MAS NMR spectrum of the sample treated with aqua regia reveals a surface with a remarkably higher concentration of terminating OH groups, accompanied by increased and alternated signal intensities in the spectral region of 4–7 ppm. Our results corroborate the substantial surface modifications upon exposure to aqua regia, and therefore support the conclusion that these superficial adaptations are the key to improved photoelectrochemical performance. In particular, the ^{1}H MAS NMR spectra do not indicate the presence of hydrogen being incorporated into the structure from NH_3 or H_2 gas used as a reactive source during synthesis. Additionally, we have performed the same experiments on the quaternary niobium-based oxynitride $SrNbO_2N$. Although the effect of increasing the concentration of surface -OH is smaller for $SrNbO_2N$ compared to $CaTaO_2N$, it is still clearly visible (Figure S4). Similar to $CaTaO_2N$, no changes could be observed in the complementary powder XRD patterns of $SrNbO_2N$ after the acid treatment (Figure S1).

The ^{14}N MAS NMR spectra exhibit a single resonance at 270 ppm (Figure 3b), in agreement with previous reports.[39,40] This signal conforms nearly perfectly to a single Lorentzian function with full width at half maximum (FMHW) of 210 Hz, which indicates an absence of any significant structural/occupational disorder. The aqua regia treatment seems to have no effect on the ^{14}N spectrum, aside from a minor increase in the baseline width of the peak. ^{14}N is an integer-spin (I = 1) nucleus which would usually display substantial resonance broadening due to the interaction between the nuclear quadrupolar moment and the electric-field gradient from the nearby electron density. However, at 60 kHz MAS the absence of spinning sidebands indicates a particularly small interaction. This is confirmed by ^{14}N NMR spectra acquired on static samples, which exhibit unusually narrow resonances with FMHW of ~1450 Hz. This indicates a quadrupolar interaction that is actually zero, due to extraordinarily high symmetry of the nitrogen site in $CaTaO_2N$, in agreement with previous studies.[39,40] Contrariwise to previous reports on Ta_3N_5 photocatalyst, we could not detect the presence of a binary TaN phase, containing partially reduced tantalum ions, in the ^{14}N MAS spectra. This suggests the origin of the photocurrent enhancement after acidic etching (*vide infra*) to be different for quaternary tantalum-based oxynitrides. The presence of any paramagnetic Ta^{4+} ions formed by reduction of Ta^{5+} during treatment with aqua regia would in principle be detectable by both ^{1}H and ^{14}N NMR, with additional peaks being observed that are shifted from the main resonances by a paramagnetic shift.[38] The absence of any such additional resonances indicates that there is no evidence for Ta^{5+} reduction.

The surface composition of the $CaTaO_2N$-A/NiB_i photoanode was investigated by XPS (Figures 3c and 3d). The Ta 4f spectrum shown in Figure 3c was deconvoluted into three doublets, which were summarized in Table 1, suggesting multiphase composition, such as Ta_3N_5, Ta_2O_5, and TaON.[39] The presence of Ta^{5+} ions surrounded by nitride and oxide anions is in agreement with the coordination of tantalum ions in $CaTaO_2N$. No peaks stemming from reduced forms of Ta^{5+} cations could be detected in the XP spectra.

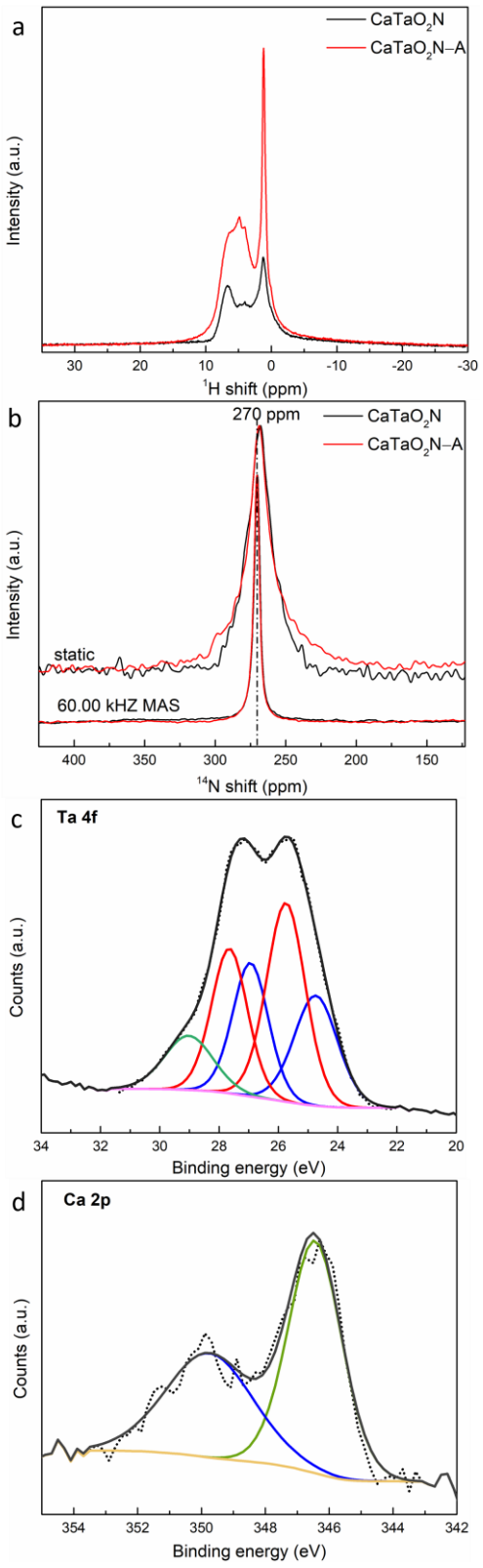

Figure 3. Solid-state NMR spectra at 60 kHz MAS of ^{1}H (a) and ^{14}N (b) for $CaTaO_2N$ powder samples before and after aqua regia treatment; XPS Ta 4f (c) and Ca 2p (d) spectra of the assembled Ti/$CaTaO_2N$-A/NiB_i photoanode (including necking treatment).

In the case of the Ca XP spectra (Figure 3d), the Ca $2p_{3/2}$ and Ca $2p_{1/2}$ peaks centered at 346.5 eV and 349.8 eV suggest the calcium atoms to be rather atoms in oxygen-hydroxide systems than in salts (e.g. carbonate, chloride, sulphate or nitrate). The E_b values of the Ca $2p_{3/2}$ peak in salts is usually in the range 347.1-348.6 eV.

Reaffirming XPS as a surface characterization technique, these results prove that the aqua regia treatment increases the concentration of terminating OH groups, even after the necking treatment. This is consistent with the ^{1}H and ^{14}N MAS NMR results (*vide supra*). The Ta 4p peak accompanied by the N 1s signal is presented in Figure S5. The low intensity of the N 1s peak at ca. 395.4 eV is probably due to the low ammonolysis temperature for the necking treatment. Due to a small surface concentration, XPS could not detect nickel from the catalytic coating. In order to investigate whether acidic treatment could change significantly the atomic Ca:Ta ratio, we performed additional XPS experiments on the pure oxynitride powder, i.e. without the Ni-B_i catalyst, before and after inserting the powder into aqua regia. Within the standard deviation of the experiment, the atomic ratio remained unchanged (Figure S6). It should be noted that the complementary Ta 4f spectrum in Figure 3c represents the composite photoanode $CaTaO_2N$-A/NiB_i where the electrocatalyst was electrochemically deposited by applying an anodic current. As such, the composite photoanode contains a relatively larger contribution of Ta^{5+} stemming from Ta_2O_5 in comparison to the XP spectra of the bare oxynitride powder presented in Figure S6.

For the complementary TEM analysis of the assembled $CaTaO_2N$-A/NiB_i photoanode, the High-Angle Annular Dark Field (HAADF) overview is shown in Figure 4a. The image reveals a large agglomerate that was mechanically removed from the electrode surface. This region was scanned and EDX data were collected at each probe position. The EDX spectra were analyzed for the presence of Ca, Ta, O, and N. Within the precision of the experiment, the agglomerate appears to be chemically homogenous. Integration over all of the EDX spectra is presented in the chart in Figure 4b. A clear peak belonging to the nickel is visible, indicating the incorporation of this element to the agglomerate. The low concentration of Ni precludes its use in for mapping with these data.

Table 1. Binding energies of Ta $4f_{5/2}$ and Ta $4f_{7/2}$ peaks for the identified Ta_3N_5, TaON, and Ta_2O_5 species.

Composition	Ta $4f_{5/2}$ (eV)	Ta $4f_{7/2}$ (eV)
Ta_3N_5	27.0	24.8
TaON	27.7	25.7
Ta_2O_5	29.1	27.0

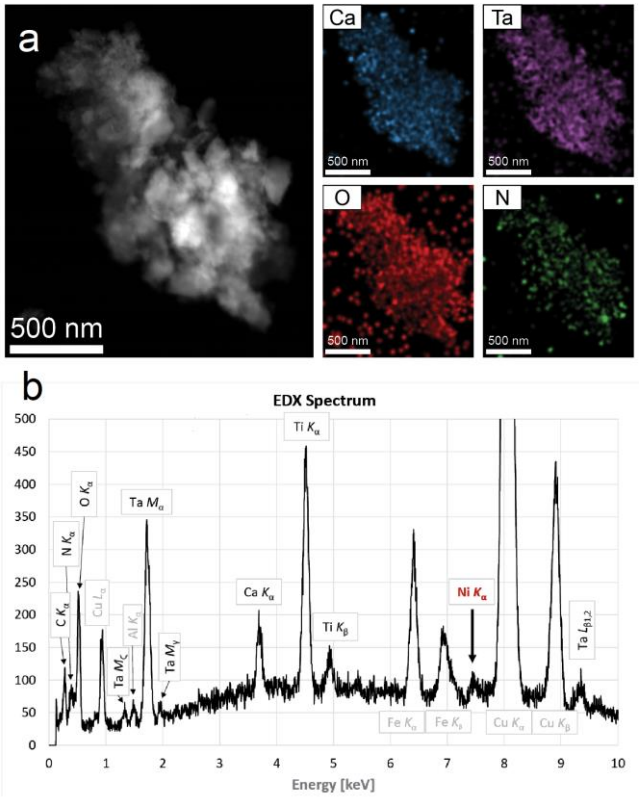

Figure 4. (a) HAADF micrograph of the Ti/$CaTaO_2N$-A/NiB_i photoanode and corresponding mapping of Ca, Ta, O and N; (b) EDX spectra from the same area of (a). Peaks of interest are labelled in black while peaks representing measurement artifacts (Cu from the TEM grid, Fe and Al from the stainless steel) are colored in gray.

Electronic structure. The ordering of oxygen and nitrogen atoms in quaternary oxynitrides is considered to have a strong effect on the photochemical properties. Hirose et al. reported the axial sites in TaO_4N_2 octahedra to be rather occupied by nitrogen than oxygen for $Ca_{1-x}Sr_xTaO_2N$ thin films.[41] We compared the bonding situation of $CaTaO_2N$ with related and photochemically-active quaternary oxynitrides $SrTaO_2N$ and $BaTaO_2N$ from our recent report.[15] There is a clear correlation between the stability of the structural model and the integrated Crystal Orbital Hamilton Population (ICOHP) values of the Ta-N interactions (Figure 5a). The ICOHP values can be interpreted as a measure of covalent strength for a certain bond.[34] This agrees well with the results of Wolff and Dronskowski who found the Ta-N responsible for the stability of the $CaTaO_2N$ structures.[30] Furthermore, we compared their structure predicted energetically to our structural models and found it to be only slightly more stable than the most stable structural model based in ref[28] (< 1 kJ/mol energy difference per unit cell).

Our most stable structural models have Ta octahedra with 2 N and 4 O in *cis* configuration. In contrast to the Ta–N interactions, there is an anti-correlation between the stability of the structural model and the ICOHP values for the Ta–O interactions. Exemplarily, COHPs for the most stable structural model are depicted in Figure 5b. As expected, only the Ta–O and Ta–N bonds are of covalent character, the Ca–O and Ca–N bonds are practically not covalent but ionic. The Ta–O bonds comprise antibonding levels below the Fermi level where the Ta–N are completely bonding. The presence of antibonding states for the Ta–O bonds and the ideal bonding situation for the Ta–N bonds is identical to the situation in $BaTaO_2N$.[15] And yet, the Ta–N bonds in $CaTaO_2N$ are even more covalent than in $BaTaO_2N$;[15] they show an ICOHP value of –5.7 eV per bond in $CaTaO_2N$ and a ICOHP value of –4.6 eV per bond in $BaTaO_2N$.[15] In contrast, the ICOHP value of the Ta-O bond in $CaTaO_2N$ is slightly less covalent than in $BaTaO_2N$ (–3.9 eV vs. –4.2 eV). With our COHP analysis, we can also confirm the Ta (5d) –N (2p) interactions to be dominating the Ta-N interactions. Kubo et al. have already detected the same findings based on charge densities.[42]

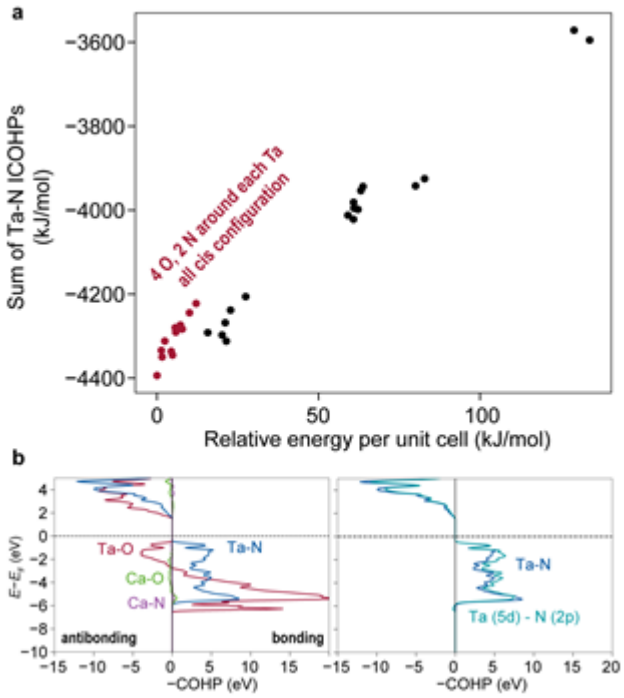

Figure 5. (a) Correlation of the energy relative to the most stable structural model to the sum of all Ta–N ICOHP values. The stability of the structural model clearly correlates with the covalent bond strengths of the Ta–N bonds; (b) depiction of the COHPs for the most stable structural model. The Ta–N bonds do not display any antibonding states below the Fermi level. In contrast, the Ta–O bonds have antibonding states below the Fermi level. The Ca–O and Ca–N interactions are nearly not covalent but mostly ionic in nature.

PEC Water Oxidation. For comparison of the PEC water oxidation activity, two separate electrodes were prepared: i) before ($CaTaO_2N$) and ii) after acidic treatment ($CaTaO_2N$-A). For both cases, post-necking treatment in the form of $TaCl_5$ impregnation followed by low-temperature ammonolysis was applied to enhance the interparticle electric conductivity.[43]

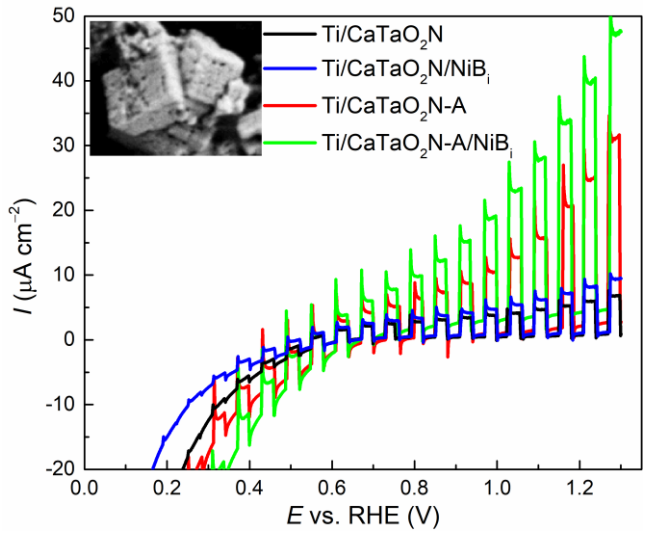

Figure 6. LSV of photoanodes $CaTaO_2N$, $CaTaO_2N$–A and composite photoanodes, containing a NiB_i catalyst, $CaTaO_2N/NiB_i$ and $CaTaO_2N$–A/NiB_i. All photoanodes were subject to necking treatment with $TaCl_5$. Measurements were performed in 0.1 M NaOH electrolyte (pH 13) at a scan rate of 10 mV s^{-1} under sequentially interrupted AM 1.5G illumination (100 mW cm^{-2}).

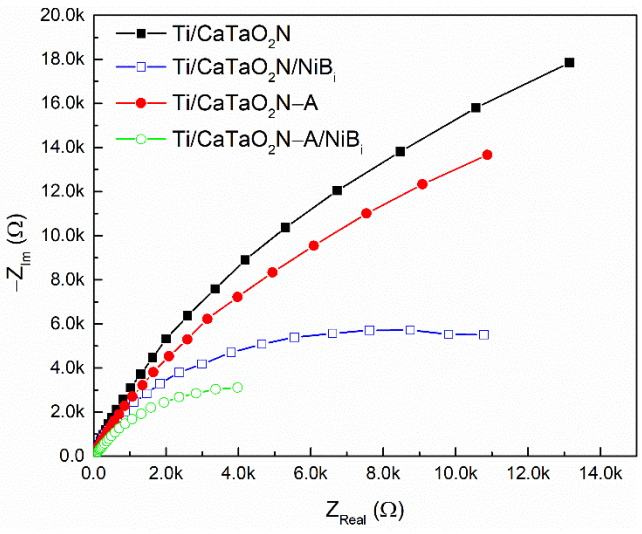

Figure 7. Nyquist plots for $CaTaO_2N$ before and after modification of photoanodes measured at 1.0 V vs RHE under AM 1.5G illumination.

The cubes were assembled into a thin film photoanode by EPD on a titanium substrate. Photoanodes on this metallic substrate without necking treatment exhibited meaningfully lower photocurrents (Figure S7). The deposition of the cubes on titanium substrates yielded higher illumination-dependent current densities in comparison to thin films on conductive fluorine-doped tin oxide (FTO) coated glass (Figure S8). This is due to the lower interfacial transfer resistance for photoelectrodes on metallic prepared substrates.[44] Nickel borate (NiB_i) was electrochemically deposited as an OER catalyst. All prepared photoanodes develop an anodic current during linear square voltammetry (LSV) under solar illumination (Figure 6). Similar to many other quaternary oxynitrides, such as $SrNbO_2N$[45], the initial photocurrent occurs at around 0.2 V vs. RHE. The initial cathodic current at low potentials has been observed previously for porous TaON on Ti substrates[46] and has been described as the capacitive current.[47] The necking treatment heightened the photocurrents in comparison to photoanodes without improvement of the interparticular electric conductivity (*vide supra*). The acidic treatment strongly enhances the current density of the $CaTaO_2N$ photoanodes. This is visible both for the photoanode with and without OER catalyst in the form NiB_i. Deposition of the catalyst improves the photocurrent due to improved reaction kinetics and a final photocurrent density of ca. 40 μA cm^{-2} is generated at 1.23 V vs RHE.[48] This is also reflected in the chronoamperometry at 1.23 V vs. RHE (Figure S9). Deposition of the catalyst on the acid-treated oxynitride gave a higher percentual upsurge of photocurrent in comparison to the pristine $CaTaO_2N$. This hints toward improved hole transfer from the light absorbing layer to the catalyst due to the acidic modification of the oxynitride surface.

EIS and Mott-Schottky measurements were carried out on the prepared photoanodes. Figure 7 depicts typical EIS Nyquist plots of the photoanodes under visible light illumination. The interface layer resistance arising at the surface of the electrode can be estimated from the arc radius of Nyquist plots; a small arc radius indicating a high charge transfer efficiency.[40] A diminished arc radius can be observed after the aqua regia treatment from Figure 7. This reduced charge transfer resistance and accelerated electron transfer induced an enhancement of anodic photocurrent (Figure 6).

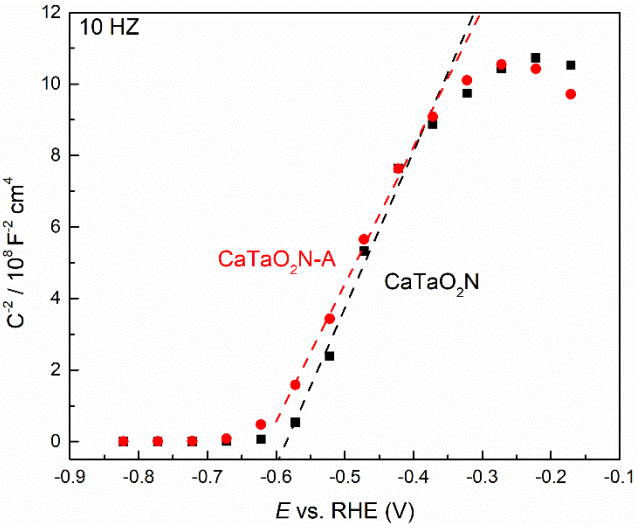

Figure 8. Mott-Schottky plot of $CaTaO_2N$ and $CaTaO_2N$-A measured at 10 Hz.

After modification with the NiB_i catalyst overlayer, both the pristine and acid-treated photoanodes exhibit a decline of the arc radius. The positive slopes of recorded Mott-Schottky plots depict that the n-type semiconducting behavior of $CaTaO_2N$ maintains after the acidic treatment (Figure 8). However, an obvious shift of the flat band po-

tential (V_{FB}) value after the aqua regia treatment can be observed. The values were −0.59 V vs RHE and −0.62 V vs RHE for the $CaTaO_2N$ and $CaTaO_2N$-A samples, respectively. Lee[41] et al. reported a change of surface band bending of p-type GaN after aqua regia treatment. This behavior could also apply for the acid-treated $CaTaO_2N$ particles.

CONCLUSION

We have determined the origin of improved photoelectrochemical activity by the acidic treatment for Ta-based quaternary oxynitrides on the example of $CaTaO_2N$. The computed electronic structure of the latter resembles $BaTaO_2N$ due to antibonding states for the Ta–O bonds and the ideal bonding situation for the Ta–N bonds. $CaTaO_2N$ has been assembled for the first time into a photoanode and the origin of ameliorated photocurrent was investigated with solid-state NMR, XPS, photoelectrochemical analysis and EIS. The ^{14}N NMR spectra indicate a high symmetry of the nitrogen signal before and after acidic treatment, while we could not detect signal stemming from other forms of (oxy)nitride phases. On the other side, ^{1}H NMR spectra suggest that photocurrent enhancement upon acidic treatment arises from a more heterogeneous surface with a significantly higher concentration of terminating OH groups. This modification enhances the charge transfer at the semiconductor-catalyst interface for the $CaTaO_2N$–A/NiB_i photoanode and yields an upsurge in photocurrent. The nature of photocurrent improvement is distinct from previous reports on $LaTiO_2N$, because a reduction of the oxidation state for the cation of the AO_4N_2 octahedra would result in the formation of inactive surface layers, such as TaN. Our results highlight the application of solid-state NMR spectroscopy for the understanding of the bulk and surface chemistry in order to develop efficient heterojunction photoanodes.

ASSOCIATED CONTENT

Supporting Information.

The Supporting Information is available free of charge on the ACS Publications website.

Powder XRD patterns of $SrNbO_2N$ before and after acid treatment; powder XRD patterns of $Ca_2Ta_2O_7$; Tauc plot for indirect allowed transition for $CaTaO_2N$ and $CaTaO_2N$-A; solid-state NMR spectra at 60 kHz MAS of ^{1}H for $SrNbO_2N$; XPS Ta 4p and N 1s spectra of the Ti/$CaTaO_2N$-A/NiB_i photoanode; XPS Ta 4f and Ca 2p spectra of the $CaTaO_2N$ powder before and after acid treatment; LSV of Ti/$CaTaO_2N$-A photoanode without necking treatment; LSV of FTO/$CaTaO_2N$ photoanode with necking treatment; Chronoamperometry of Ti/$CaTaO_2N$ and Ti/$CaTaO_2N$-A photoanode with necking treatment and NiB_i.

AUTHOR INFORMATION

Corresponding Author

* (A.S.) E-mail adam.slabon@mmk.su.se.

Author Contributions

All authors have given approval to the final version of the manuscript.

ACKNOWLEDGMENT

Z. M. would like to thank the China Scholarship Council for a Ph.D. scholarship. T. T. acknowledges funding from the Swedish Research Council (Project No. 2016-05113). The XPS measurements were carried out with the equipment purchased with the financial support of the European Regional Development Fund in the framework of the Polish Innovation Operational Program (contract no. POIG.02.01.00-12-023/08). J.G. acknowledges the F.R.S.-FNRS project HTBaSE (Contract No. PDR-T.1071.15) for financial support. A. J. and A. J. P. were supported by the Swedish Research Council (Project no. 2016-03441). We acknowledge the Consortium des Équipements de Calcul Intensif en Fédération Wallonie Bruxelles (CÉCI) for computational resources. We thank Birgit Hahn for acquiring SEM images and Ricarda Pütt for UV-vis measurements. This work was performed, in part, at Electron Microscopy Centre supported by Department of Materials and Environmental Chemistry and Faculty of Science at Stockholm University.

REFERENCES

(1) Wang, S.; Liu, G.; Wang, L. Crystal Facet Engineering of Photoelectrodes for Photoelectrochemical Water Splitting. *Chem. Rev.* **2019**, *119*, 5192–5247.

(2) Saadi, F. H.; Lewis, N. S.; McFarland, E. W. Relative Costs of Transporting Electrical and Chemical Energy. *Energy Environ. Sci.* **2018**, *11*, 469–475.

(3) Nocera, D. G. Solar Fuels and Solar Chemicals Industry. *Acc. Chem. Res.* **2017**, *50*, 616–619.

(4) Davi, M.; Drichel, A.; Mann, M.; Scholz, T.; Schrader, F.; Rokicinska, A.; Kustrowski, P.; Dronskowski, R.; Slabon, A. Enhanced Photoelectrochemical Water Oxidation Efficiency of $CuWO_4$ Photoanodes by Surface Modification with Ag_2NCN. *J. Phys. Chem. C* **2017**, *121*, 26265–26274.

(5) Davi, M.; Mann, M.; Ma, Z.; Schrader, F.; Drichel, A.; Budnyk, S.; Rokicinska, A.; Kustrowski, P.; Dronskowski, R.; Slabon, A. An MnNCN-Derived Electrocatalyst for $CuWO_4$ Photoanodes. *Langmuir* **2018**, *34*, 3845–3852.

(6) Liu, C.; Tang, J.; Chen, H. M.; Liu, B.; Yang, P. A Fully Integrated Nanosystem of Semiconductor Nanowires for Direct Solar Water Splitting. *Nano Lett.* **2013**, *13*, 2989–2992.

(7) Sivula, K.; Formal, F. Le; Grätzel, M. WO_3–Fe_2O_3 Photoanodes for Water Splitting: A Host Scaffold, Guest Absorber Approach. *Chem. Mater.* **2009**, *21*, 2862–2867.

(8) Davi, M.; Ogutu, G.; Schrader, F.; Rokicinska, A.; Kustrowski, P.; Slabon, A. Enhancing Photoelectrochemical Water Oxidation Efficiency of WO_3/α-Fe_2O_3 Heterojunction Photoanodes by Surface Functionalization with CoPd Nanocrystals. *Eur. J. Inorg. Chem.* **2017**, *2017*, 4267–4274.

(9) Sougrati, M. T.; Arayamparambil, J. J.; Liu, X.; Mann, M.; Slabon, A.; Stievano, L.; Dronskowski, R. Carbodiimides as Energy Materials: Which Directions for a Reasonable Future? *Dalt. Trans.* **2018**, *47*, 10827–10832.

(10) Fuertes, A. Synthetic Approaches in Oxynitride Chemistry. *Prog. Solid State Chem.* **2018**, *51*, 63–70.

(11) Liu, G.; Ye, S.; Yan, P.; Xiong, F.; Fu, P.; Wang, Z.; Chen, Z.; Shi, J.; Li, C. Enabling an Integrated Tantalum Nitride Photoanode to Approach the Theoretical Photocurrent Limit for Solar Water Splitting. *Energy Environ. Sci.* **2016**, *9*, 1327–1334.

(12) Seo, J.; Nishiyama, H.; Yamada, T.; Domen, K. Visible-Light-Responsive Photoanodes for Highly Active, Stable Water Oxidation. *Angew. Chemie - Int. Ed.* **2018**, *57*, 8396–8415.

(13) Davi, M.; Schrader, F.; Scholz, T.; Ma, Z.; Rokicinska, A.; Dronskowski, R.; Kustrowski, P.; Slabon, A. $SrTaO_2N$ Nanowire Photoanode Modified with a Ferrihydrite Hole-Storage Layer for Photoelectrochemical Water Oxidation. *ACS Appl. Nano Mater.* **2018**, *1*, 869–876.

(14) Jiang, Y.; Liu, P.; Chen, Y.; Zhou, Z.; Yang, H.; Hong, Y.; Li, F.; Ni, L.; Yan, Y.; Gregory, D. H. Construction of Stable Ta_3N_5/g-C_3N_4 Metal/Non-Metal Nitride Hybrids with Enhanced Visible-Light Photocatalysis. *Appl. Surf. Sci.* **2017**, *391*, 392–403.

(15) Ma, Z.; Thersleff, T.; Görne, A. L.; Cordes, N.; Liu, Y.; Jakobi, S.; Rokicinska, A.; Schichtl, Z. G.; Coridan, R. H.; Kustrowski, P.; et al. Quaternary Core–Shell Oxynitride Nanowire Photoanode Containing a Hole-Extraction Gradient for Photoelectrochemical Water Oxidation. *ACS Appl. Mater. Interfaces* **2019**, *11*, 19077–19086.
(16) Matsukawa, M.; Ishikawa, R.; Hisatomi, T.; Moriya, Y.; Shibata, N.; Kubota, J.; Ikuhara, Y.; Domen, K. Enhancing Photocatalytic Activity of $LaTiO_2N$ by Removal of Surface Reconstruction Layer. *Nano Lett.* **2014**, *14*, 1038–1041.
(17) Wang, C.; Hisatomi, T.; Minegishi, T.; Wang, Q.; Zhong, M.; Katayama, M.; Kubota, J.; Domen, K. Synthesis of Nanostructured $BaTaO_2N$ Thin Films as Photoanodes for Solar Water Splitting. *J. Phys. Chem. C* **2016**, *120*, 15758–15764.
(18) Nurlaela, E.; Ould-Chikh, S.; Harb, M.; del Gobbo, S.; Aouine, M.; Puzenat, E.; Sautet, P.; Domen, K.; Basset, J.-M.; Takanabe, K. Critical Role of the Semiconductor–Electrolyte Interface in Photocatalytic Performance for Water-Splitting Reactions Using Ta_3N_5 Particles. *Chem. Mater.* **2014**, *26*, 4812–4825.
(19) Sasaki, R.; Maeda, K.; Kako, Y.; Domen, K. Preparation of Calcium Tantalum Oxynitride from Layered Oxide Precursors to Improve Photocatalytic Activity for Hydrogen Evolution under Visible Light. *Appl. Catal. B Environ.* **2012**, *128*, 72–76.
(20) Xu, J.; Pan, C.; Takata, T.; Domen, K. Photocatalytic Overall Water Splitting on the Perovskite-Type Transition Metal Oxynitride $CaTaO_2N$ under Visible Light Irradiation. *Chem. Commun.* **2015**, *51*, 7191–7194.
(21) Higashi, M.; Abe, R.; Takata, T.; Domen, K. Photocatalytic Overall Water Splitting under Visible Light Using $ATaO_2N$ (A = Ca, Sr, Ba) and WO_3 in a IO_3^-/I^- Shuttle Redox Mediated System. *Chem. Mater.* **2009**, *21*, 1543–1549.
(22) Yoshitomi, F.; Sekizawa, K.; Maeda, K.; Ishitani, O. Selective Formic Acid Production via CO_2 Reduction with Visible Light Using a Hybrid of a Perovskite Tantalum Oxynitride and a Binuclear Ruthenium(II) Complex. *ACS Appl. Mater. Interfaces* **2015**, *7*, 13092–13097.
(23) Jansen, M.; Letschert, H. P. Inorganic Yellow-Red Pigments without Toxic Metals. *Nature* **2000**, *404*, 980–982.
(24) Dang, K.; Chang, X.; Wang, T.; Gong, J. Enhancement of Photoelectrochemical Oxidation by an Amorphous Nickel Boride Catalyst on Porous $BiVO_4$. *Nanoscale* **2017**, *9*, 16133–16137.
(25) Hwang, T.; van Zijl, P. C. M.; Garwood, M. Fast Broadband Inversion by Adiabatic Pulses. *J. Magn. Reson.* **1998**, *133*, 200–203.
(26) Kervern, G.; Pintacuda, G.; Emsley, L. Fast Adiabatic Pulses for Solid-State NMR of Paramagnetic Systems. *Chem. Phys. Lett.* **2007**, *435*, 157–162.
(27) Pell, A. J.; Pintacuda, G. Broadband Solid-State MAS NMR of Paramagnetic Systems. *Prog. Nucl. Magn. Reson. Spectrosc.* **2015**, *84–85*, 33–72.
(28) Günther, E.; Hagenmayer, R.; Jansen, M. Strukturuntersuchungen an Den Oxidnitriden $SrTaO_2N$, $CaTaO_2N$ Und $LaTaON_2$ Mittels Neutronen- Und Röntgenbeugung. *Z. Anorg. Allg. Chem.* **2000**, *626*, 1519–1525.
(29) Ong, S. P.; Richards, W. D.; Jain, A.; Hautier, G.; Kocher, M.; Cholia, S.; Gunter, D.; Chevrier, V. L.; Persson, K. A.; Ceder, G. Python Materials Genomics (Pymatgen): A Robust, Open-Source Python Library for Materials Analysis. *Comput. Mater. Sci.* **2013**, *68*, 314–319.
(30) Wolff, H.; Dronskowski, R. First-Principles and Molecular-Dynamics Study of Structure and Bonding in Perovskite-Type Oxynitrides ABO_2N (A = Ca, Sr, Ba; B = Ta, Nb). *J. Comput. Chem.* **2008**, *29*, 2260–2267.
(31) Blöchl, P. E. Projector Augmented-Wave Method. *Phys. Rev. B* **1994**, *50*, 17953–17979.
(32) Kresse, G.; Joubert, D. From Ultrasoft Pseudopotentials to the Projector Augmented-Wave Method. *Phys. Rev. B* **1999**, *59*, 1758–1775.
(33) Perdew, J. P.; Burke, K.; Ernzerhof, M. Generalized Gradient Approximation Made Simple. *Phys. Rev. Lett.* **1996**, *77*, 3865–3868.
(34) Dronskowski, R.; Blöchl, P. E. Crystal Orbital Hamilton Populations (COHP): Energy-Resolved Visualization of Chemical Bonding in Solids Based on Density-Functional Calculations. *J. Phys. Chem.* **1993**, *97*, 8617–8624.
(35) Deringer, V. L.; Tchougréeff, A. L.; Dronskowski, R. Crystal Orbital Hamilton Population (COHP) Analysis as Projected from Plane-Wave Basis Sets. *J. Phys. Chem. A* **2011**, *115*, 5461–5466.
(36) Maintz, S.; Deringer, V. L.; Tchougréeff, A. L.; Dronskowski, R. Analytic Projection from Plane-Wave and PAW Wavefunctions and Application to Chemical-Bonding Analysis in Solids. *J. Comput. Chem.* **2013**, *34*, 2557–2567.
(37) Maintz, S.; Deringer, V. L.; Tchougréeff, A. L.; Dronskowski, R. LOBSTER: A Tool to Extract Chemical Bonding from Plane-Wave Based DFT. *J. Comput. Chem.* **2016**, *37*, 1030–1035.
(38) Reimer, J. A. Development of NMR: Solid-state NMR and Materials Science, Post 1995. *eMagRes* **2012**, *1*, 457-472.
(39) Kim, Y.-I.; Paik, Y. Bond Covalency in Perovskite Oxynitrides $ATaO_2N$ (A = Ca, Sr, Ba) Studied by ^{14}N NMR Spectroscopy. *Solid State Sci.* **2012**, *14*, 580–582.
(40) Cordes, N.; Bräuniger, T.; Schnick, W. Ammonothermal Synthesis of $EAMO_2N$ (EA = Sr, Ba; M = Nb, Ta) Perovskites and ^{14}N Solid-State NMR Spectroscopic Investigations of AM $(O,N)_3$ (A = Ca, Sr, Ba, La). *Eur. J. Inorg. Chem.* **2018**, *2018*, 5019–5026.
(41) Oka, D.; Hirose, Y.; Matsui, F.; Kamisaka, H.; Oguchi, T.; Maejima, N.; Nishikawa, H.; Muro, T.; Hayashi, K.; Hasegawa, T. Strain Engineering for Anion Arrangement in Perovskite Oxynitrides. *ACS Nano* **2017**, *11*, 3860–3866.
(42) Kubo, A.; Giorgi, G.; Yamashita, K. Anion Ordering in $CaTaO_2N$: Structural Impact on the Photocatalytic Activity. Insights from First-Principles. *Chem. Mater.* **2017**, *29*, 539–545.
(43) Landsmann, S.; Maegli, A. E.; Trottmann, M.; Battaglia, C.; Weidenkaff, A.; Pokrant, S. Design Guidelines for High-Performance Particle-Based Photoanodes for Water Splitting: Lanthanum Titanium Oxynitride as a Model. *ChemSusChem* **2015**, *8*, 3451–3458.
(44) Tawfik, W. Z.; Hassan, M. A.; Johar, M. A.; Ryu, S.; Lee, J. K. Highly Conversion Efficiency of Solar Water Splitting over p-Cu_2O/ZnO Photocatalyst Grown on a Metallic Substrate. *J. Catal.* **2019**, *374*, 276–283.
(45) Maeda, K.; Higashi, M.; Siritanaratkul, B.; Abe, R.; Domen, K. $SrNbO_2N$ as a Water-Splitting Photoanode with a Wide Visible-Light Absorption Band. *J. Am. Chem. Soc.* **2011**, *133*, 12334–12337.
(46) Higashi, M.; Tomita, O.; Abe, R. Porous TaON Photoanodes Loaded with Cobalt-Based Cocatalysts for Efficient and Stable Water Oxidation Under Visible Light. *Top. Catal.* **2016**, *59*, 740–749.
(47) Ziani, A.; Nurlaela, E.; Dhawale, D. S.; Silva, D. A.; Alarousu, E.; Mohammed, O. F.; Takanabe, K. Carrier Dynamics of a Visible-Light-Responsive Ta_3N_5 Photoanode for Water Oxidation. *Phys. Chem. Chem. Phys.* **2015**, *17*, 2670–2677.
(48) Mavrokefalos, C.; Patzke, G. Water Oxidation Catalysts: The Quest for New Oxide-Based Materials. *Inorganics* **2019**, *7*, 29.

TOC Graphic

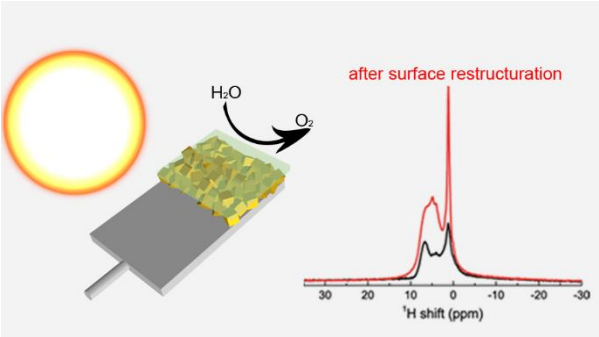
H₂O
O₂
after surface restructuration
30
20
10
0
-10
-20
-30
¹H shift (ppm)